AIAA Aviation
16-20 June 2014, Atlanta, GA
20th AIAA/CEAS Aeroacoustics Conference

Sound Radiated From a Rotor and Its Relation to Rotating Frame Measurements of Ingested Turbulence

W. Nathan Alexander[1], William Devenport[2], and David Wisda[3]
Virginia Tech, Blacksburg VA 24061

Michael A. Morton[4]
Naval Air Warfare Center Aircraft Division, Patuxent River MD 20670

Stewart A. L. Glegg[5]
Florida Atlantic University, Boca Raton FL 33431

Broadband haystacking noise results from the correlated unsteady loading of successive blades due to ingested turbulence. This noise can therefore be predicted with knowledge of the turbulent inflow and blade response function, but this is not trivial, especially for complex flows which are inhomogeneous and anisotropic. This paper details the noise and direct measurement of the unsteady upwash correlation from the rotating frame of a 10-bladed 457 mm diameter rotor immersed in two planar wall boundary layers of varying thickness at non-thrusting and thrusting advance ratios. At low thrust conditions, the measured upwash correlation can be predicted using the fixed frame space-time correlation function. However, as the thrust is increased the predictions progressively deviate from measurement most likely due to the formation of a separation region generated on the wall beneath the rotor. Surprisingly, this produces haystacking-like behavior in rotor-frame measurements of the blade-to-blade upwash correlation at spanwise locations near the blade tips. A lateral contraction of the turbulence is not observed in measurement of the spanwise coherence with increasing thrust. Finally, the spectral peaks in the radiated noise increase with the boundary layer thickness by similar ratios at low thrust conditions. For high thrust, the peaks in the broadband noise have the same approximate magnitude.

I. Introduction

Broadband sound generated by a rotor ingesting turbulence can appear drastically different than that of an isolated airfoil because of the possibility of adjacent blades producing correlated unsteady loads when they encounter large scale turbulence. The blade-to-blade correlation produces a far field broadband noise spectrum characterized by haystacking. Haystacking was first observed by Sevik (1971) from a rotor ingesting grid turbulence. Sevik's tests were conducted at a low thrust condition and a force balance was used to measure the unsteady lift projected in the axial direction. Measurements were compared to predictions of the blade loading response, which took into account the turbulence correlation function. The haystacking peaks in the spectrum that were measured at the blade passage frequency (BPF) and its harmonics, were absent in the prediction because it omitted the possibility of blade-to-blade coherent loading.

Hanson (1974) and Majumdar and Peake (1998) analyzed turbulence noise ingestion at static and flight conditions. Majumdar and Peake (1998) show that at flight conditions, in which the ingested turbulence is near isotropic, the blade-to-blade correlation may be negligible. However, when the inflow conditions caused the turbulence to be stretched in the axial direction, both Hanson (1974) and Majumdar and Peake (1998) showed that haystacking would be expected. With the development of advanced aircraft design concepts, such as the hybrid wing-body, which have the engines buried in the suction side boundary layer of the vehicle, the ingested turbulence can no longer be considered isotropic. In this case, the ingested flow is inhomogeneous, anisotropic, and may be significantly distorted.

[1] Research Scientist, Department of Aerospace and Ocean Engineering, AIAA Member.
[2] Professor, Department of Aerospace and Ocean Engineering, AIAA Associate Fellow.
[3] Graduate Student, Department of Aerospace and Ocean Engineering, AIAA Student Member.
[4] Test Engineer, AIAA Member
[5] Professor, Department of Ocean Engineering, AIAA Associate Fellow.

Glegg *et al.* (2013) show that the sound spectrum generated by a rotor with *B* blades is given by

$$S_{pp}(\mathbf{x},\omega)=\frac{1}{4\pi T}\sum_{n=1}^{B}\sum_{m=1}^{B}\int_{R_{\min}}^{R_{\max}}\int_{R_{\min}}^{R_{\max}}\int_{-T}^{T}\int_{-T}^{T}\left\{\frac{\partial}{\partial x_i}\frac{n_i^{(n)}(R,\tau)e^{i\omega r^{(n)}(\tau)/c_o}}{4\pi r^{(n)}(\tau)}\right\}\left\{\frac{\partial}{\partial x_i}\frac{n_j^{(m)}(R,\tau')e^{-i\omega r^{(m)}(\tau')/c_o}}{4\pi r^{(m)}(\tau')}\right\}R_{FF}^{(n,m)}(R,R',\tau,\tau')e^{i\omega(\tau-\tau')}dRdR'd\tau d\tau' \tag{1}$$

where n_i is the blade normal, *n,m* identify each blade in the rotor, *R* is the radial location on the blade, and $r(\tau)$ is the distance from each blade element to the observer specified at source time τ. The blade-to-blade loading correlation function $R_{FF}^{(n,m)}$ can be related to the correlation function of the unsteady upwash $R_{ww}^{(n,m)}$ as

$$R_{FF}^{(n,m)}(R,R',\tau,\tau')=\int_{-\infty}^{\tau}\int_{-\infty}^{\tau}s(R,\tau-\tau_o)s(R',\tau'-\tau_o)R_{ww}^{(n,m)}(R,R',\tau_o,\tau_o')d\tau_o d\tau_o' \tag{2}$$

where $R_{ww}^{(n,m)}$ is the correlation function of the upwash velocity between blades *n* and *m*. Providing that R_{ww} is known, these integrals can be evaluated numerically in the time domain.

Morton *et al*. (2012) investigated the coherent turbulent structure ingested by a rotor immersed in a thick, high Reynolds number turbulent boundary layer. He presents measurement of the full 4-dimensional space-time correlation function from a 101 mm thick boundary layer developed on a wall of the Virginia Tech Stability Wind Tunnel test section. His correlation measurements show a large scale turbulent correlation structure inclined approximately 30º to the wall. He analyzed the unsteady upwash correlations that would be expected by a rotor cutting through this correlation function and found an asymmetry in blade-to-blade correlations. The blade-to-blade correlations were largest for an interior point along a leading blade's span and a point further towards the tip on a successive blade. This was due to the 30° inclination of the space-time correlation structure. If the radial distances were reversed on successive blades the correlation was significantly reduced. Morton *et al.* (2012) used a frequency domain analysis which ignored turbulence distortion at thrusting conditions to predict the far field noise of the rotor. Glegg *et al.* (2013) advanced the analysis by using the calculated correlations to predict far field haystacking noise at thrusting conditions by applying a modified form of Rapid Distortion Theory suitable for use in a sheared flow to account for the distortion of inflow turbulence. Their results agreed well with the coinciding acoustic measurements of Alexander *et al.* (2013) showing that the haystacks narrow as the turbulence is stretched at thrusting conditions.

The analysis given in Equations 1 and 2 does not account for the distortion of the turbulence and the non-linear evolution of the flow under the influence of the rotor alone unless included directly in the unsteady upwash correlation. Accurate representation of the function R_{ww} is therefore vital to predicting the rotor noise. The objective of the present study is to analyze these issues through measurements of the upwash seen from the rotor-blades themselves, as well as the sound the rotor produces. In this paper, we present direct rotating frame measurements of the turbulent upwash field experienced by a rotor and the spanwise and blade-to-blade coherence of that upwash turbulence responsible for the resultant haystacking noise. Comparisons are made with predictions using Morton *et al.*'s (2012) turbulence data, which neglect the effect of distortion, and with the radiated sound field over a broad range of operating conditions.

II. Apparatus and Instrumentation

A. Wind Tunnel

This experiment was conducted in the Virginia Tech Stability Wind Tunnel. Figure 1 shows a diagram of the wind tunnel test section and experiment set-up. The tunnel, in its anechoic configuration, has an acoustically treated test section with Kevlar acoustic windows on the starboard and port walls that contain the flow. For this study, the starboard Kevlar wall was replaced with six hard Lexan panels that could be adjusted to a zero pressure gradient. The test section wall was 7.32m long. A thick high Reynolds number boundary layer was grown on this wall for ingestion into the rotor which was positioned 3.41m from the beginning of the test section. The boundary layer was tripped in the contraction section using two different trip configurations to produce a 101 mm thick or 186 mm thick

boundary layer. The boundary layer thicknesses were approximately invariant for the studied inflow velocities: 10m/s, 15m/s, 20m/s, and 30m/s. Full two-point cross-sectional turbulent velocity correlation measurements were completed and are presented in Morton (2012). Table 1 shows the measured boundary layer characteristics as presented in Morton (2012) for the two trip configurations with a free stream velocity of U=30m/s at the location of the rotor disk plane.

Table 1. Boundary layer characteristics at the rotor disk plane with the rotor removed

δ, mm	U, m/s	C_f	δ^*, mm	θ, mm	Re_δ	Re_θ
101	30	0.00258	11.6	9.2	182,890	16,607
186	30	0.00245	19.3	15.9	345,660	29,475

B. Rotor

The rotor used in this study is a 2.25 scale version of Sevik's (1971) 10-blade open rotor. Figure 2 shows the rotor mounted in the anechoic test section of the Virginia Tech Stability Wind Tunnel. The blades are near symmetric, without skew, lean, or sweep, have square tips and a constant chord of 57.2mm. The blade pitch varies from 55.6º at the root to 21.2º at the tip. The rotor diameter is 457 mm and the hub diameter is 127 mm. The hub was expanded slightly beyond a scale version of the Sevik's rotor by eliminating the interior 6.35 mm of the blade roots to make room for on-board instrumentation. The design advance ratio is 1.17 and the zero-thrust condition was calculated with JavaProp to be at an advance ratio of 1.44. The spinner extends 216.4 mm in front of the root of the blades. The rotor was powered with a Kollmorgen AKM-64P-ACCNDA00 servo-motor controlled by a S61200 servo-drive. The rotor was positioned close to the wall with a 20.3mm blade tip gap so that the outer 50% of the blade span was immersed in the 101 mm thick boundary layer and 100% of the blade span was immersed in the 186 mm thick boundary layer. Test matrices of the measured conditions are shown in Figure 3 for both hotwire and acoustic measurements. This extensive list includes 305 individual on-blade two-point hotwire correlation measurements and 105 separate acoustic runs.

C. Microphones

Microphone measurements were made over an arc extending from 15° to 165° to the rotor axis using an array of Bruel & Kjaer model 4190 ½-inch microphones. Data presented in this paper were obtained from an upstream inflow position at a receiving angle of 15º to the axis of rotation as shown in Figure 1, 2.23 m from the point of rotation in the rotor disk plane. The microphone was held by an aerodynamically faired stand suspended from the ceiling designed to limit aerodynamically produced noise. The microphone was fitted with a Bruel & Kjaer nose cone model UA-0386. Data acquisition was performed using a Bruel & Kjaer LAN-XI modular DAQ sampling at 65536Hz for 32 seconds. Spectral data are the combined average of 511 records of 8192 samples each. Sound measurements were made at identical conditions both with and without on-blade hot-wire probes, discussed below, present. The presence of the hotwires produced additional noise, but the general haystacking form was comparable to the noise from the unmodified blades. Therefore, only noise from the clean blades (without probes) will be presented and compared with the turbulence measurements.

D. Hotwires

Six total cross-wire probes were bonded to the pressure side of two blades of the rotor to measure the two-component velocity statistics of the mean inflow and upwash velocities. Potential flow theory was used to determine a sufficient distance upstream to position the probes which would be outside of the influence of the blade. The measurement volumes of the probes were positioned 19 mm in front of the lead of the rotor blades. Four probes were on a leading blade at 98.5%, 95%, 90%, and 80% of the blade radius. An immediately succeeding blade had two probes at 98.5% and 90% radius. Figure 4 shows the on-blade hotwire configuration. A custom-built 4-channel constant voltage anemometer system designed by Tao Systems was installed in the nose cone which spun with the model. The output voltages of the bridge were relayed to the fixed frame by a Moog high speed low noise slip ring Model AC6231 for measurement by a NI DAQ model USB-6211. The hotwire signals were phase locked with the clocking signal from a laser/photodiode system. The laser was pointed at the nose cone which had a mirror at a single location to reflect the laser onto a photodiode once per revolution. Data were recorded at 51200Hz for 30 seconds. Due to channel limitations on the slip ring, only two cross-wire probe pairs could be operated simultaneously. Therefore, correlation measurements between probe pairs had to be done one pair at a time and were manually switched between runs. Seven different probe combinations were measured as listed in Table 2. The probe signals were analyzed independently for self-coherence to identify spectral peaks due to electrical interference as the

signal from the random turbulence should not have significant coherence over large time delay. Each signal was filtered to remove the contribution of this noise. Most signals contained a 60 Hz interference which was removed, except in cases where the BPF was a close multiple of 60. In these cases, the 60 Hz noise could not be filtered from the data. Instead, the spectra were manually interpolated across the 60 Hz spike.

Table 2. Cross-wire probe correlation pairs in percent radius (L=leading blade, T=trailing blade)

98.5% L to 90%T
95%L to 98.5%T
95%L to 90%T
90%L to 90%T
80%L to 90%T
95%L to80%L
98.5%L to 95%L

E. Flow Visualization

Tuft flow visualization was used to observe the streamlines approaching and underneath the disk plane in the vicinity of the wall for several advance ratios. Black lights positioned in the test section across from the rotor on the test section floor were used to illuminate Danville's Flymaster 6/0 waxed fluorescent yellow 0.05 mm diameter fly fishing thread. Pictures were taken with a Canon Rebel T3 camera positioned outside of the test section behind the Lexan wall. Tufts were positioned approximately every 48 mm with only the initial 12 mm of the string taped to the wall with clear tape.

III. Results and Discussion

The results and discussion are separated into two parts. First, the effect of thrust on both the sound and ingested turbulence will be presented. Then, the effect of increasing the boundary layer thickness, and subsequently the maximum possible size of the ingested turbulent structures, will be analyzed. In both sections, selected data representative of the entire test matrix are presented in order to clearly describe the observed trends.

i. Influence of Thrust

Figure 5a shows the background-subtracted noise measured from the rotor operating at various thrusting conditions with a constant freestream velocity of 20 m/s in the 101 mm boundary layer. At high thrusting conditions (low J) five harmonics of the blade passage frequency are visible. The blade passage frequency increases with RPM as well as the broadband magnitude. In Figure 5b, the haystacking spectral shapes are compared by scaling the spectra on the freestream tip velocity, U_e, to the fifth power (standard dipole efficiency) and the blade passage frequency. As thrust increases the haystacks become narrow and the peak magnitudes increase. They also become more symmetric about the BPF and its harmonics. This is consistent with results found in previous studies (Majumdar and Peake (1998), Martinez (1996)) and is an effect of the stretching of turbulent eddies. This effect can also be seen in the acoustic contour plots of Wisda *et al.* (2014) which show the noise produced by this rotor over a large range of advance ratios. As the rotor thrust is increased the boundary layer turbulence is stretched into long filaments. These filaments are ingested into the rotor and are cut many times producing a correlated loading response. Although the effect of the turbulence distortion is easily observed in the measured noise, direct measurement of the turbulent distortion as seen by the rotor blades is more difficult. For accurate broadband noise prediction, the distorted turbulent inflow must be well understood. For a rotor operating in an open environment, the distortion effects can be closely approximated for accurate sound prediction using Rapid Distortion Theory, but for more complex cases as discussed here in which the distortion is inhomogeneous and the flow is wall-bounded, the distortion is not easily predictable.

To directly measure the distortion, two of the rotor blades were outfitted with cross-wire probes over the outer 80% of their span. Figure 6 shows the measured unsteady upwash correlation as seen by probe pairs on the two successive blades and across their span at a zero-thrust condition. The correlation spectra were computed by averaging record lengths of 8192 samples measured at 51216.4 Hz. Upwash, in this case, is defined as velocity normal to the airfoil chord. The upwash correlation between successive blades is responsible for the broadband haystacking noise. The largest blade-to-blade correlations are observed between a position at 95% radius on the leading blade and a location at 98.5% radius on the trailing blade. This coincides with the inclined turbulent structures present in the boundary layer as shown in the measurements of Morton (2012). The spanwise correlation

along a single blade between the outer most positions is also very high peaking at $\gamma^2 = \frac{G_{xy}G_{yx}^*}{G_{xx}G_{yy}} = 0.75$. These outermost spanwise positions are separated by 8.1 mm. In all blade-to-blade cases, the coherence begins to roll-off near the BPF since this is the frequency associated with the space-time delay between two successive blades. Disturbances at frequencies above the BPF are less likely to be correlated because their spatial extents in the plane of the blade trace are less than the spacing between successive blades. The coherence is insignificant at frequencies greater than the second harmonic of the BPF. Predictions of the unsteady upwash spectra as calculated from the undisturbed boundary layer measurements of Morton (2012) are shown as thick dashed lines in comparison to the measurements. The predictions are calculated by simulating the upwash seen by various locations along the span of the rotor blades essentially cutting the measured correlation function along different oblique planes. The upwash frequency correlation spectra between two points on the rotor can be written in terms of the space-time correlation function as in Equation 3.

(3)

$$S_{ww}^{(n,k)}(\omega, R, R') = \frac{1}{4\pi^2}\frac{\pi}{T}\int_{-T}^{T}\int_{-T}^{T} n_i^{(n)}(R,\tau)\, n_j^{(k)}(R',\tau')\, R_{ij}\left(\mathbf{z}_n(\tau), \mathbf{z}_k(\tau'), \tau-\tau'\right) e^{i\omega(\tau-\tau')} d\tau\, d\tau'$$

$n_i^{(n)}$ is the blade n normal component at spanwise position R at time delay τ and R_{ij} is the measured stationary frame normalized space-time correlation function

The predicted correlations were computed to match the sampling scheme of the measured data. The integrations extend over a time period covering multiple revolutions, 4.9 rotations for the 1823 RPM case presented in Figure 6. The predictions are adjusted to include 6.7 revolutions for the 2500 RPM cases which will be presented later. The predictions also sample the space-time correlation function at an equivalent rate to match the measurement sampling frequency. These predictions compare well with measurement validating this method of calculating coherent loading response for the zero-thrust condition but do not take into account any flow distortion or other rotor effects that are necessary for accurate sound prediction for cases with significant turbulence distortion.

Figure 7 shows similar measured and predicted correlations for conditions of increasing thrust. For all cases, as the thrust is increased the lumps at the frequency of revolution, visible at multiples of f/BPF=10^{-1}, become more pronounced. This is consistent with an increasing number of cuts into a coherent structure by the same blade on successive rotations. The predictions, which account for the varying inflow and rotational velocities, also show this phenomenon, but the effect is minimized most likely because the predictions do not consider any flow distortion. For the lightly thrusting condition J=1.05, the predictions represent the average magnitude of the distorted flow quite well although do not display the same ridges at the rotational frequency. As the thrust is increased further, the coherence measured for the 95%L to 98.5%T pair begins to display a phenomenon at the BPF and its harmonics which is not reproduced by the predictions. At J = 0.52, this feature becomes noticeable in the 90%L to 90%T spectrum, although to a lesser extent. For all blade-to-blade probe pair combinations in the outer 10% of the blade span, the correlations increased with thrust.

Interestingly, the spanwise single blade correlations remain relatively constant with increasing thrust instead of decreasing as might be expected if eddies were laterally contracting while being distorted. This result, although confusing, is supported by the lateral scale analysis conducted in Alexander *et al.* (2013) which used the mean acoustic spectra haystacking decay to determine lateral turbulence scales and Wisda *et al.* (2014) which computed an integral time-scale from the autocorrelation function of phase-averaged eddy acoustic signatures. These studies found that the lateral integral scale does not diminish with advance ratio and remains approximately 35 mm for all thrusting conditions.

The phase-average unsteady upwash can be plotted as a disk plane contour map to observe the mean distortion of the turbulent boundary layer into the rotor face. Figure 8 shows the root mean squared unsteady upwash velocity contours as seen by the rotor blades for four different thrusting conditions. The mean velocity components have been removed in these plots. In all cases, including zero thrust (J=1.44), the velocity contours are not symmetric and are swept upward into the path of the downstroke of the rotor blades. This may result from the induced velocity produced by the individual rotor blades as they pass through the slower moving boundary layer fluid. Even at a freestream zero-thrust condition, the blades will produce lift when passing through the boundary layer. Also, the contour maps show as the thrust is increased, the region of highest unsteady upwash becomes concentrated at the bottom of the rotation nearest the wall.

The reason for the concentration of unsteady flow near the wall can be observed in the tuft flow visualizations. Figure 9 shows the near wall flow is separating 0.5δ upstream of the rotor for the high thrust case (J = 0.58). The flow downstream and underneath the disk plane is reversed and turns back toward the rotor axis. Visualizations completed at advance ratios from 1.44 to 0.48 incrementing by 0.096 indicate that the separation and flow reversal starts to occur on the wall around J = 0.86. This behavior may explain the broadband peak at the BPF and its harmonics shown in the blade upwash correlations in Figure 7. The tip vortex may be pushed back into the rotor plane by the reverse flow causing a blade vortex interaction on successive blades.

To emphasize the effects of this detachment on the rotor upwash, Figure 10a shows an RMS upwash profile taken through the three highest advance ratio contours of Figure 8 at bottom dead center in the boundary layer compared to the upwash profile determined from the undisturbed boundary layer measurement of Morton (2012). Although the measured upwash profiles are overpredicted by the profile produced from the undisturbed boundary layer measurement, the shape and magnitudes are similar. Figure 10b shows the data in Figure 10a but also includes the J=0.58 case as well. The jump in RMS unsteady upwash for this case is drastic increasing beyond the undisturbed values by over 2.5 fold. The separation region on the wall becomes thick and disrupts the upwash profile over the outer 10% radius of the blade tip.

The hotwire and flow visualization analyses show the rotor moving through very different flow regimes which will have a large impact on the prediction of the far field noise. Rapid Distortion Theory that only distorts the upstream turbulence by a defined steady flow would be unable to predict the noise produced by the ingestion of the separated boundary layer flow.

ii. Influence of Boundary Layer Thickness

Noise and coherence spectra were also measured for the rotor operating in a thicker, 186 mm, boundary layer. In this case, the entire span of a blade when at bottom dead center is immersed in the boundary layer. Background-subtracted noise spectra are plotted in Figure 11a. Additional acoustic contour maps showing the noise variation with advance ratio are given in Wisda *et al.* (2014). The axes of Figure 11b have been normalized on the blade passage frequency and freestream velocity to the fifth power as before in Figure 5. The results are qualitatively similar to those from the thinner 101 mm boundary layer. As J decreases the haystacks narrow and become symmetric about the BPF. More information on the noise source can be derived from direct comparison of the noise produced by ingestion of the two different boundary layers. Figure 12 shows the noise recorded for two similar operating conditions varying only the boundary layer thickness. The sound is increased by the thicker boundary layer for the zero thrust case, but has little impact on the high thrust (low J) case. This difference could be due to the separation phenomenon observed in the coherence measurements and the flow visualization. The dominant noise source for the low advance ratio case is a function of the turbulence ingested from the separation region and not the incoming boundary layer turbulence. Interestingly, at higher J, the increase in noise increases by the same factor as the boundary layer thickness. The ratio of boundary layer thickness is 1.84, which is equivalent to an increase of $10\log_{10}(1.84)$= 2.65 dB.

Coherence measurements were only completed for a single probe combination in the thicker boundary layer. These probes were on the same blade at 98.5% and 95% radius. Figure 13 shows the measured coherence at several operating conditions along with the results from the thinner boundary layer and predictions that include the increased boundary layer thickness. The coherence at low frequency (f/BPF<1) is increased for the thicker boundary layer. This makes qualitative sense since the thicker boundary layer contains larger eddies and therefore more low frequency content directly associated with the incoming boundary layer structure. The prediction accurately accounts for the increased coherence at low frequency. The difference in measured coherence for the low frequency region between the two boundary layers is less for the highest thrust case. This suggests again that the dominant correlation mechanism in this regime may be separation and flow reversal of the wall boundary layer and not eddy structures ingested from the upstream boundary layer. Also, for high frequencies (f/BPF>1), the prediction agrees well with the measurement at high advance ratios near zero thrust. As thrust is increased, the prediction tends to decay similarly with non-dimensional frequency while the measured coherence decays less rapidly. The same trend can be observed in measurements from the 101 mm thick boundary layer.

IV. Conclusions

Noise and aerodynamic measurements were completed for a 457.2 mm diameter 10-bladed rotor operating near a planar wall with a tip gap of 20.7 mm. Boundary layers of varying thickness, 101 mm and 186 mm, were generated on the wall by varying the size of upstream trips. The blade-to-blade upwash correlation at several spanwise positions along consecutive blades was directly measured at multiple operating conditions and compared to

predictions attained from a fixed frame space-time correlation measurement of the undisturbed boundary layer. Noise was also measured and analyzed with the aerodynamic results.

Broadband haystacking noise was measured, and the haystacks narrow, increase in magnitude, and become more symmetric about the blade passage frequency and its harmonics as the thrust is increased. The character of this noise can be predicted with knowledge of the complete unsteady upwash correlation function as shown by Glegg *et al.* (2013), but this is not trivial for a wall bounded flow. For zero-thrust and lightly thrusting cases, the unsteady upwash coherence spectra are accurately predicted using measurement of the undisturbed boundary layer. This predictive analysis accounts for changes in freestream velocity, rotational velocity, and boundary layer thickness, but does not correct for turbulence distortion as the correlation matrix is assumed frozen and convected through the disk plane of the rotor. As the thrust is increased, peaks arise at the harmonics of the rotational rate of the rotor corresponding to multiple cuts of the same eddy. The predictions become progressively worse with increasing thrust. At advance ratios below 0.79, the measured blade-to-blade coherence at the tip of the blade has its own haystacking-like feature present at the BPF and its harmonics. This may be a result of boundary layer separation and flow reversal as observed by the tuft flow visualization. Unfortunately, this is an effect not predictable by applying Rapid Distortion Theory to the measured undisturbed boundary layer correlation function.

The measured turbulence correlations also show that the distortion does not behave as would be expected in a stream tube contraction in a free field environment. The spanwise coherence spectra vary only slightly with increased thrust. They do not exhibit a lateral contraction in the form of reduced low frequency coherence as would be expected for simple stretching of a vortex filament. This observation agrees with findings of Alexander *et al.* (2013) which used the mean haystacking noise spectral decay to determine lateral turbulence scales.

Disk plane contours show the maximum root mean squared unsteady upwash velocities occur on the downstroke of the rotor blades. The unsteady upwash is not symmetric in the boundary layer. These contours also show a region of very high upwash velocity nearest the wall at low advance ratios indicating that the flow is separated from the wall for these conditions. The root mean-squared unsteady upwash is insignificant outside of the boundary layer for all conditions.

Increasing the boundary layer thickness increases the maximum size of ingested turbulent eddies. This influences the predicted and measured unsteady upwash spectra by increasing the amount of correlated low frequency content. The measured haystacking peaks at higher advance ratios increase by a ratio similar to that of the increased boundary layer thickness. For lower advance ratios at which the noise is most likely due to the ingested turbulence from the separated boundary layer, the magnitude of the spectral peaks agree for both boundary layers.

Acknowledgments

The authors would like to thank the Office of Naval Research, in particular Drs. Ki-Han Kim and John Muench, for their support under grants N00014-10-1-0908 and N00014-14-1-0141.

References

Alexander, W. N., Devenport, W., Morton, M. A., and Glegg, S. A. L., "Noise from a Rotor Ingesting a Planar Turbulent Boundary Layer", 19th AIAA/CEAS Aeroacoustics Conference, AIAA-2013-2285, Berlin, DE, May 27-29, 2013.

Glegg, S. A. L., Kawashima, E., Lachowski, F., Devenport, W., and Alexander, N., "Inflow Distortion Noise in a Non Axisymmetric Flow", 19th AIAA/CEAS Aeroacoustics Conference, AIAA-2013-2286, Berlin, DE, May 27-29, 2013.

Hanson, D., "Spectrum of Rotor Noise Caused by Atmospheric Turbulence", *Journal of the Acoustical Society of America*, vol. 56, 1974, pp. 110-126.

Majumder, S. and Peake, N., "Noise Generation by the Interaction between Ingested Turbulence and a Rotating Fan", *Journal of Fluid Mechanics*, vol. 359, 1998, pp. 181-216.

Martinez, R., "Asymptotic Theory of Broadband Rotor Thrust, Part II: Analysis of the Right Frequency Shift of the Maximum Response", *Journal of Applied Mechanics*, vol. 63, 1996, pp. 143-148.

Morton, M. A., "Rotor Inflow Noise Caused by a Boundary Layer: Inflow Measurements and Noise Predictions", Master's Thesis, AOE Department, Virginia Tech, Blacksburg, VA, 2012. Avail: http://scholar.lib.vt.edu/theses/available/etd-08102012-103032/.

Morton, M., Devenport, W., Alexander, W.N., Glegg, S.A.L., and Borgoltz, A., "Rotor Inflow Noise Caused by a Boundary Layer: Inflow Measurements and Noise Predictions", 18th AIAA/CEAS Aeroacoustics Conference, AIAA-2012-2120, Colorado Springs, CO, June 4-6, 2012.

Wisda, D., Alexander, W.N., Devenport, W., and Glegg, S. A. L., "Boundary Layer Ingestion Noise and Turbulence Scale Analysis at High and Low Advance Ratios", *to be presented at the 20th AIAA/CEAS Aeroacoustics meeting in Atlanta, Georgia June 16-20, 2014.*

Sevik, M., "Sound Radiation from a Subsonic Rotor Subjected to Turbulence", NASA SP 304, 1971.

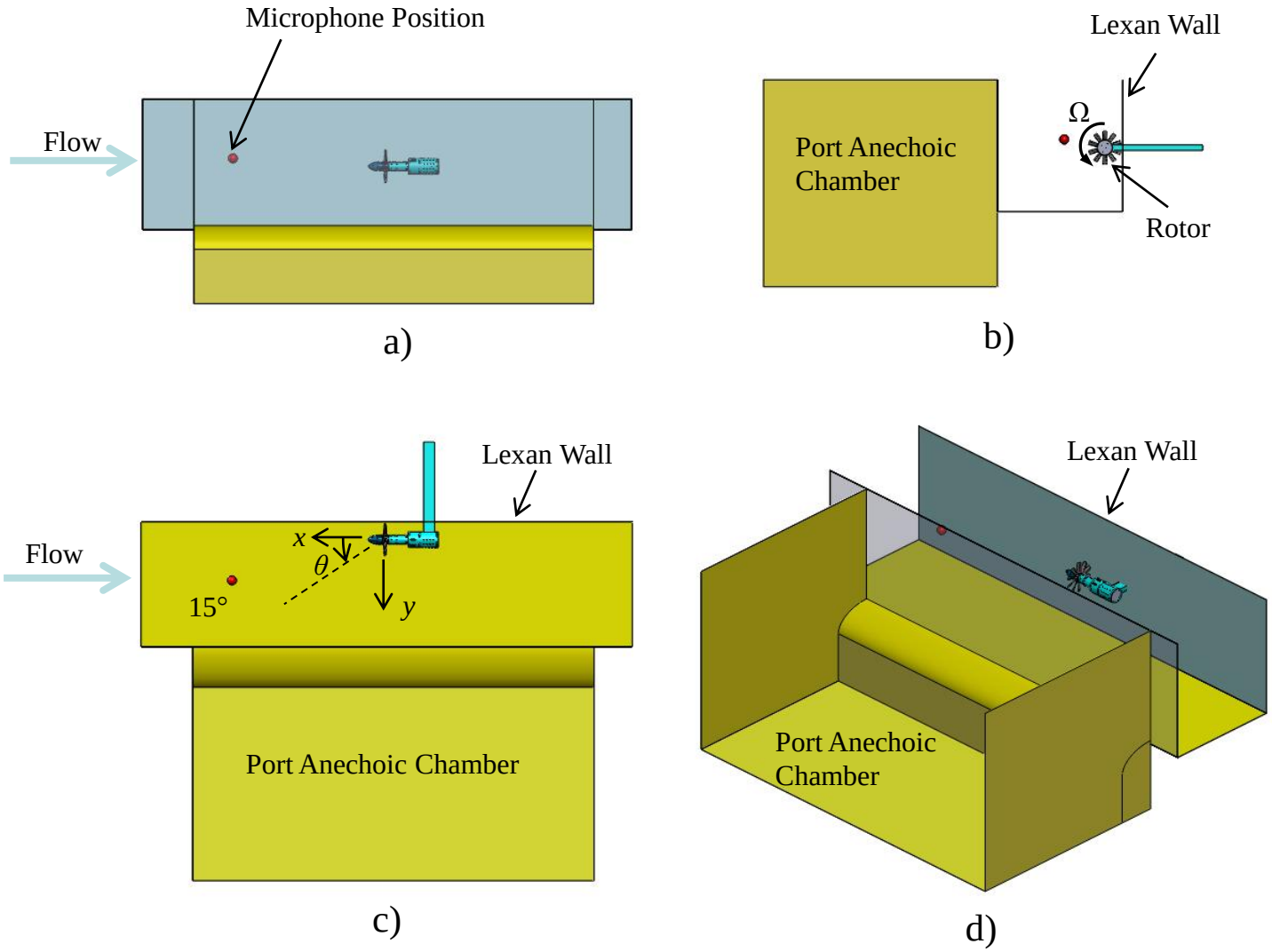

Figure 1. Diagram of Virginia Tech Stability Tunnel anechoic test section and rotor position

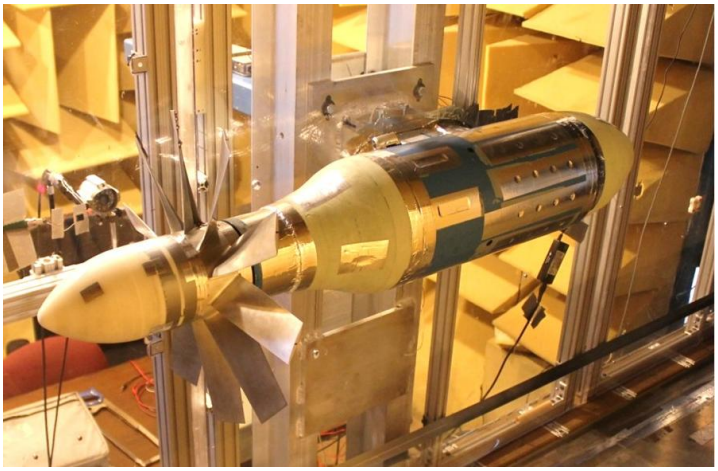

Figure 2. Rotor mounted in the Virginia Tech Stability Wind Tunnel

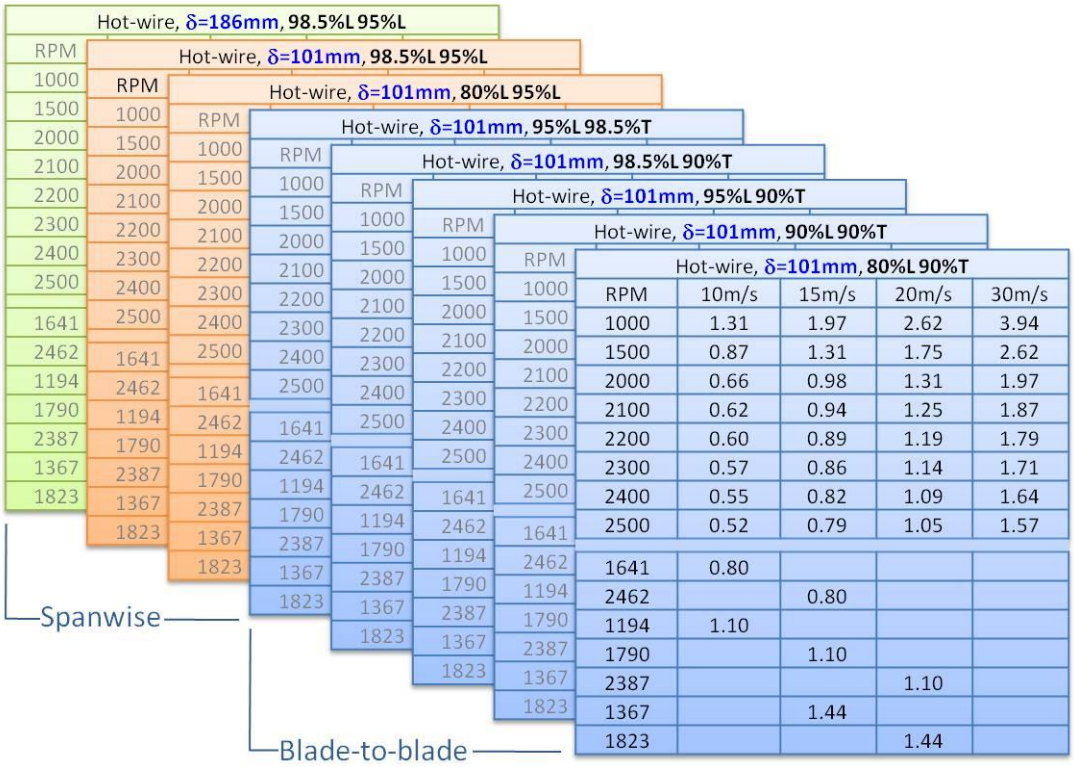

RPM	10m/s	15m/s	20m/s	30m/s
1000	1.31	1.97	2.62	3.94
1500	0.87	1.31	1.75	2.62
2000	0.66	0.98	1.31	1.97
2100	0.62	0.94	1.25	1.87
2200	0.60	0.89	1.19	1.79
2300	0.57	0.86	1.14	1.71
2400	0.55	0.82	1.09	1.64
2500	0.52	0.79	1.05	1.57
1641	0.80			
2462		0.80		
1194	1.10			
1790		1.10		
2387			1.10	
1367		1.44		
1823			1.44	

a)

Sound measurements 2734rpm, δ=101mm	
10m/s	0.48
12m/s	0.58
14m/s	0.67
16m/s	0.77
18m/s	0.86
20m/s	0.96
22m/s	1.06
24m/s	1.15
26m/s	1.25
28m/s	1.34
30m/s	1.44
32m/s	1.54
34m/s	1.63
Directivity angles from 15° to 168°	

	Sound measurements, δ=101mm			
RPM	10m/s	15m/s	20m/s	30m/s
1000	1.31	1.97	2.62	3.94
1500	0.87	1.31	1.75	2.62
2000	0.66	0.98	1.31	1.97
2100	0.62	0.94	1.25	1.87
2200	0.60	0.89	1.19	1.79
2300	0.57	0.86	1.14	1.71
2400	0.55	0.82	1.09	1.64
2500	0.52	0.79	1.05	1.57
2750	0.48	0.72	0.95	1.43
3000	0.44	0.66	0.87	1.31
3250	0.40	0.61	0.81	1.21
3500	0.37	0.56	0.75	1.12
3750	0.35	0.52	0.70	1.05
4000	0.33	0.49	0.66	0.98
4250	0.31	0.46	0.62	0.93
4500	0.29	0.44	0.58	0.87
3282			0.8	
1194	1.10			
1790		1.10		
2387			1.10	
3581				1.10
1367		1.44		
1823			1.44	
2734				1.44
Directivity angles from 15° to 168°				

	Sound measurements, δ=186mm			
RPM	10m/s	15m/s	20m/s	30m/s
1000	1.31	1.97	2.62	3.94
1500	0.87	1.31	1.75	2.62
2000	0.66	0.98	1.31	1.97
2100	0.62	0.94	1.25	1.87
2200	0.60	0.89	1.19	1.79
2300	0.57	0.86	1.14	1.71
2400	0.55	0.82	1.09	1.64
2500	0.52	0.79	1.05	1.57
2750	0.48	0.72	0.95	1.43
3000	0.44	0.66	0.87	1.31
3250	0.40	0.61	0.81	1.21
3500	0.37	0.56	0.75	1.12
3750	0.35	0.52	0.70	1.05
4000	0.33	0.49	0.66	0.98
4250	0.31	0.46	0.62	0.93
4500	0.29	0.44	0.58	0.87
3282			0.8	
1194	1.10			
1790		1.10		
2387			1.10	
3581				1.10
1367		1.44		
1823			1.44	
2734				1.44
Directivity angles from 15° to 168°				

b)

Figure 3. Test matrix for a) on-blade two-point hotwire correlation measurements for positions on a leading (L) and trailing (T) blade at different spanwise positions listed as percent of rotor radius b) and acoustic measurements

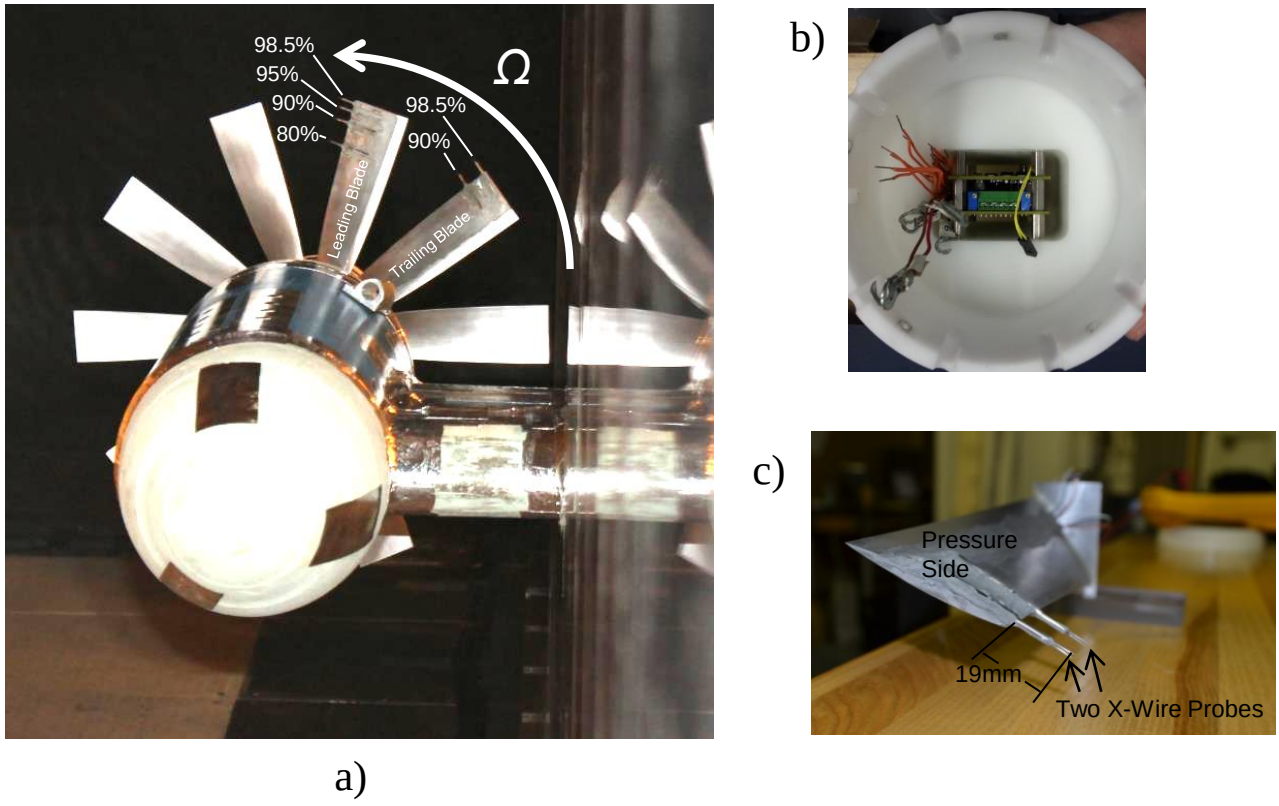

Figure 4. Hotwire system a) blade mounted probes, b) CVA bridge in the nose cone, c) and close-up view of probes on a blade

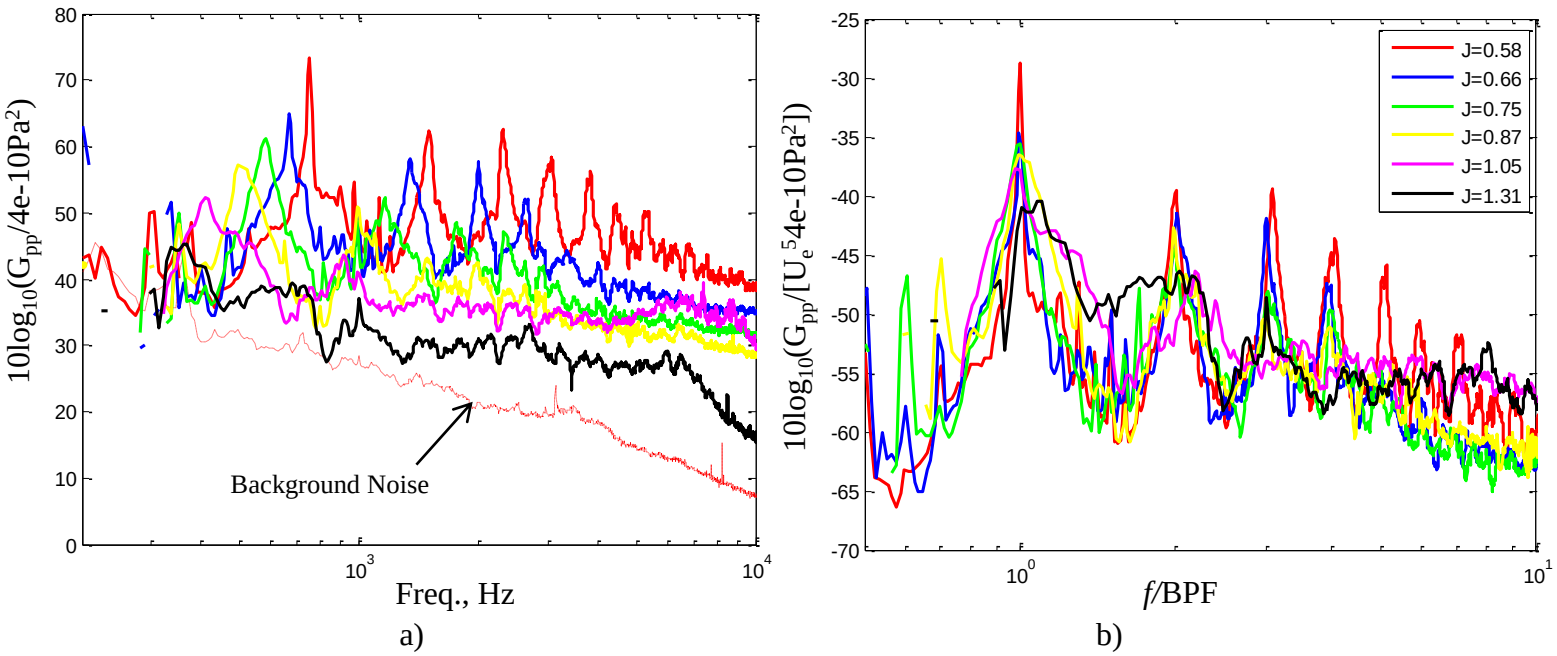

Figure 5. Haystacking noise from rotor measured from θ=15° with an inflow velocity of 20m/s

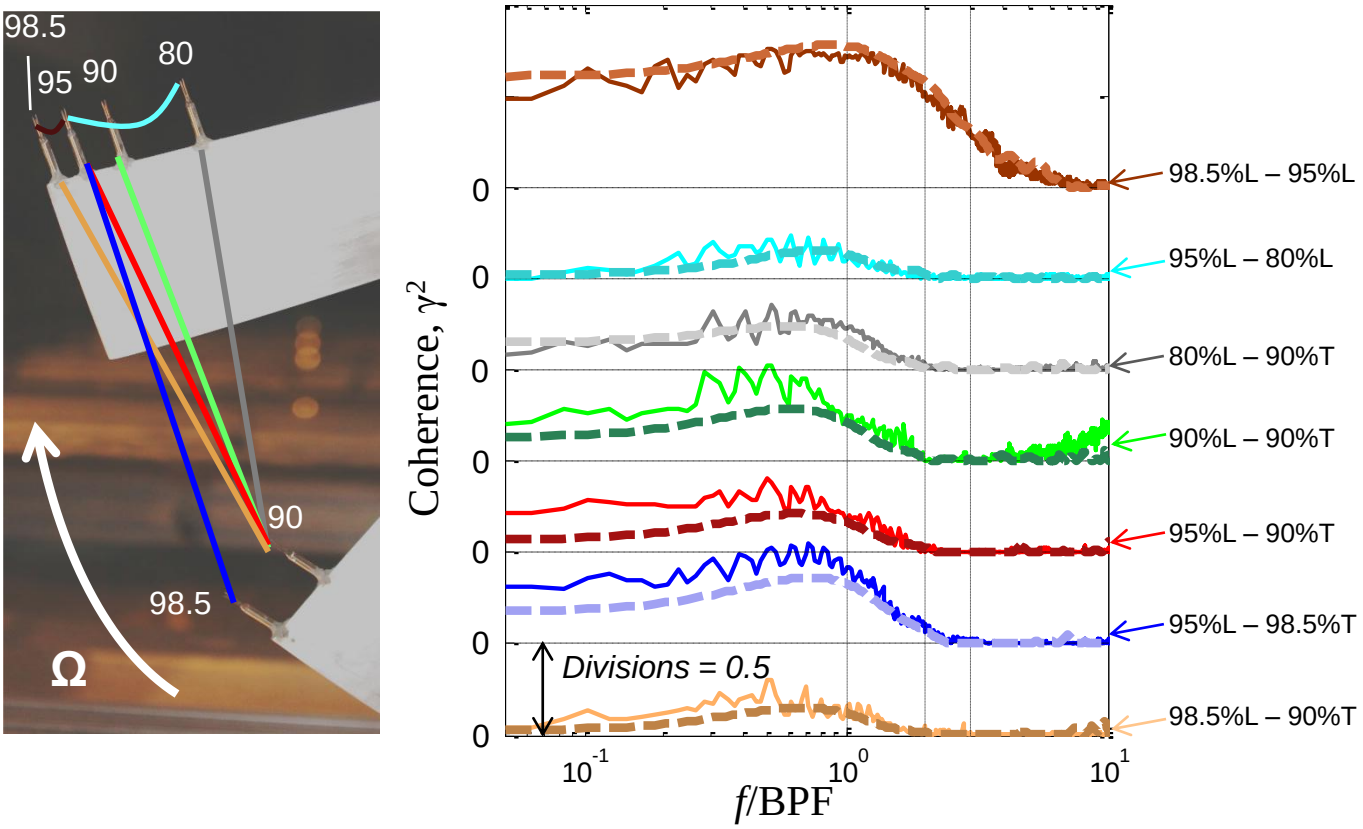

Figure 6. Blade-to-blade coherence for different probe pairs at a zero-thrust condition, J=1.44, 20m/s, 1823RPM. (Predictions shown as dashed lines, L=leading blade, T=trailing blade)

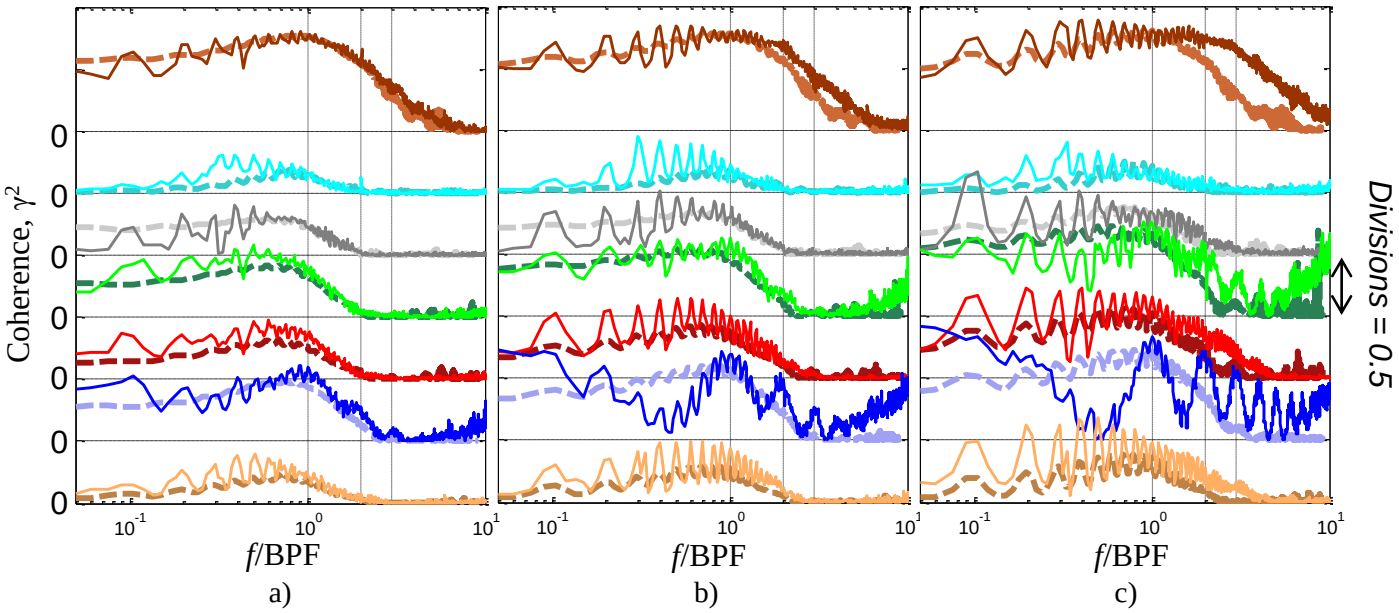

Figure 7. Blade-to-blade coherence for different probe pairs at a) J=1.05, 20m/s, 2500RPM, b) J=0.79, 15m/s, 2500RPM, c) J=0.52, 10m/s, 2500RPM. (Predictions shown as dashed lines, colors correspond to Figure 6)

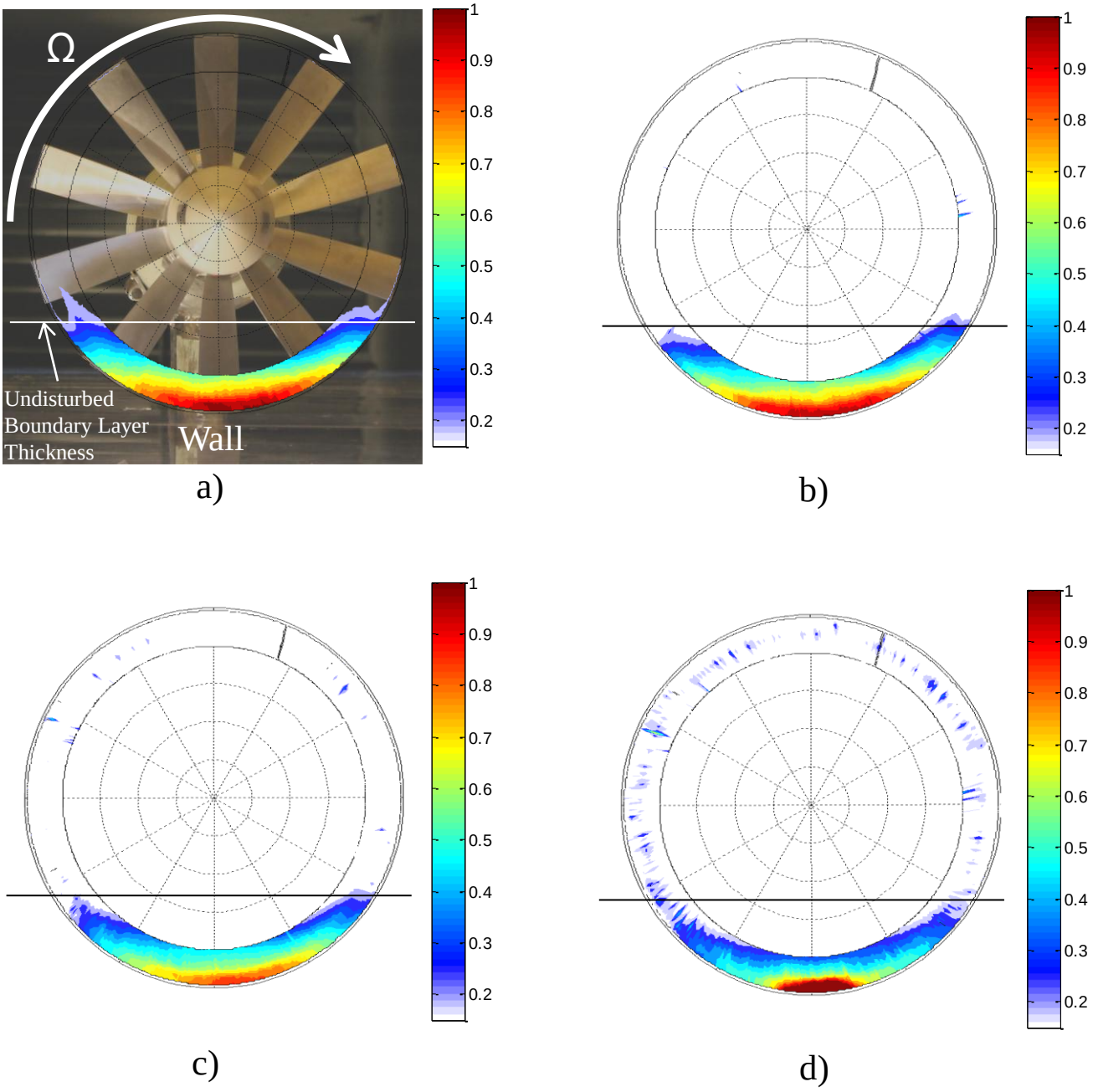

Figure 8. Root mean-squared unsteady upwash for the outer 80% of the blade radius in m/s as seen by the rotor blades in the disk plane for a) J=1.44, b) J=1.05, c) J=0.79, d) J=0.52

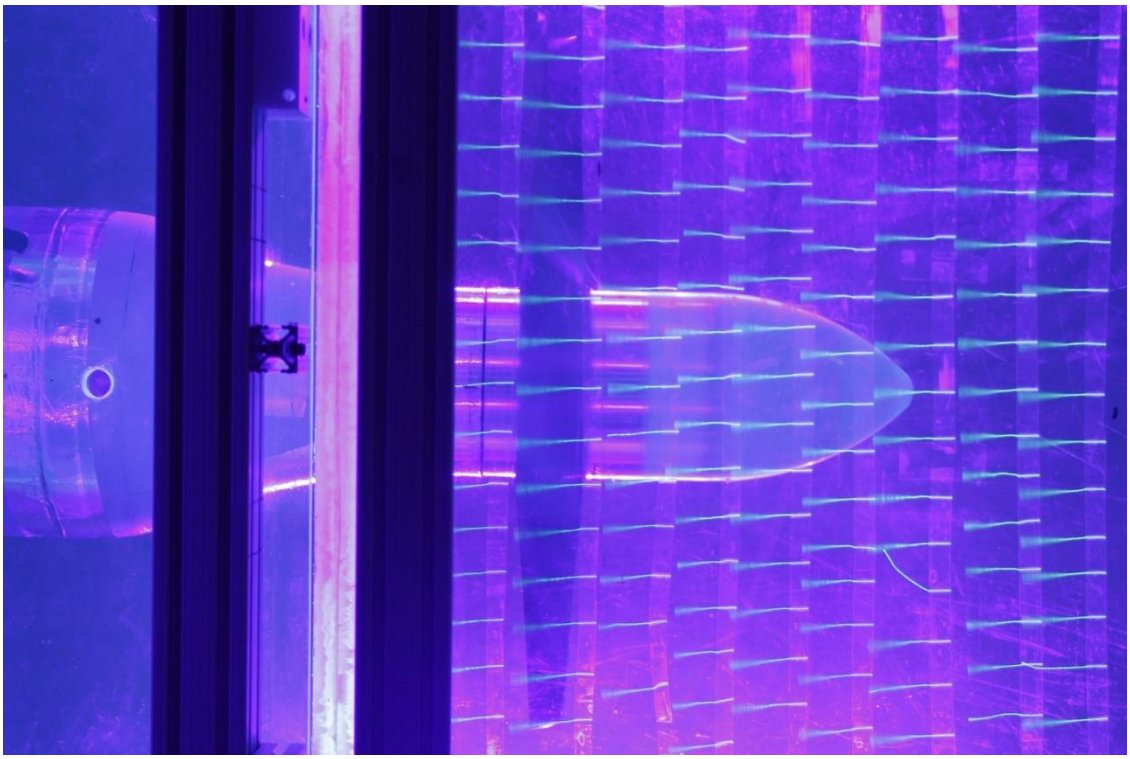

a)

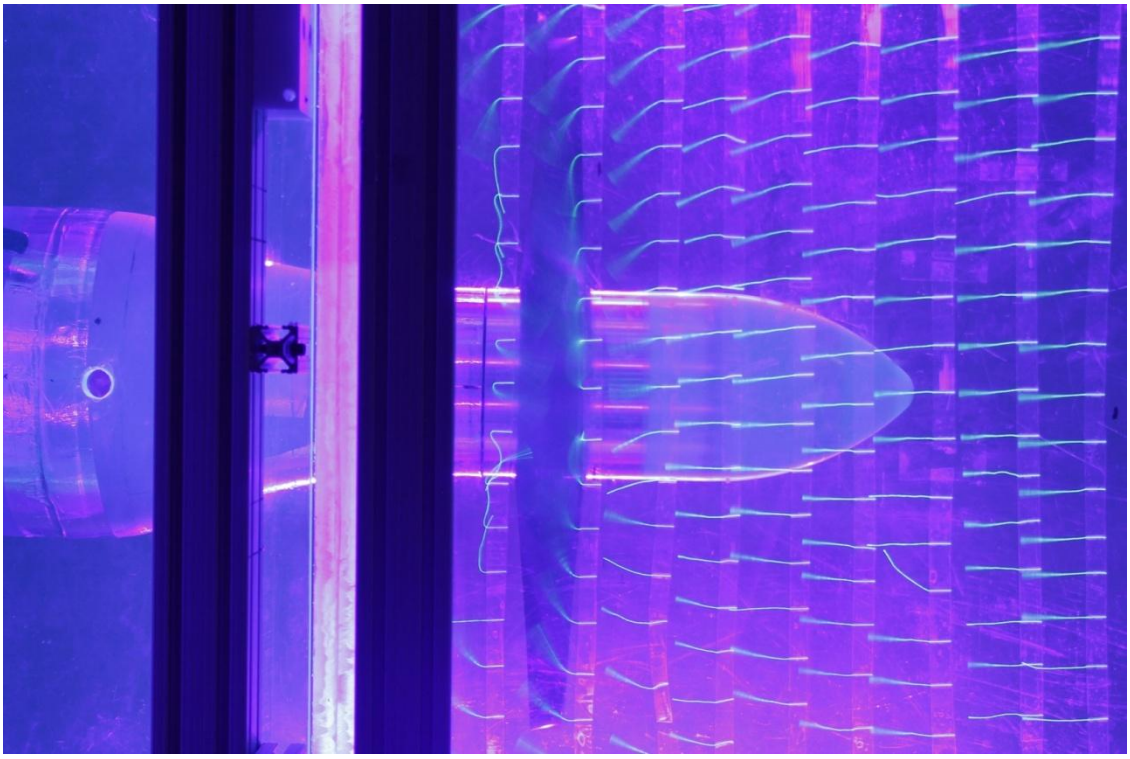

b)

Figure 9.Tuft flow visualization at a) J=1.44 and b) J=0.58

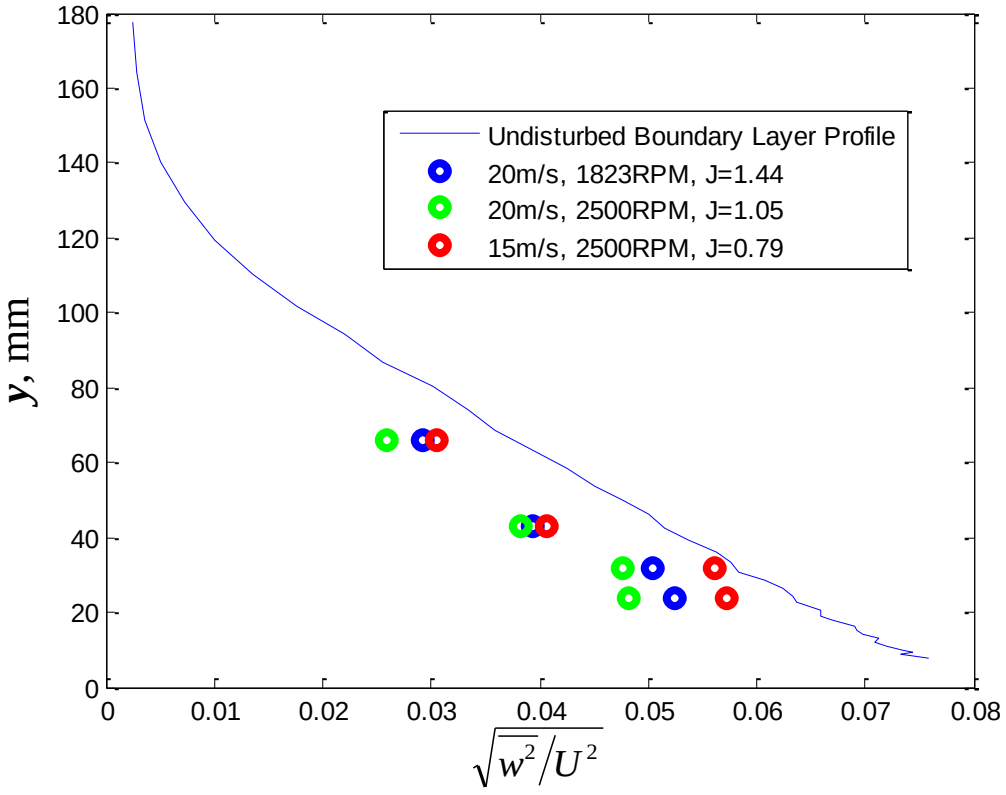

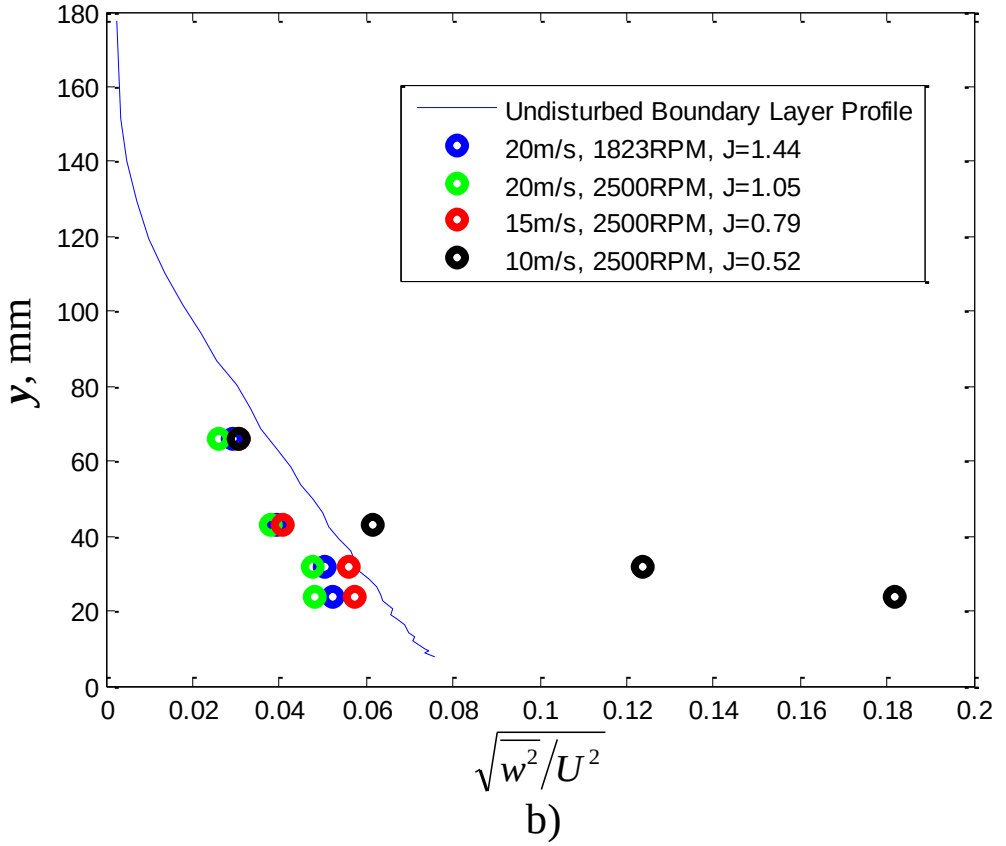

Figure 10. Profiles of the unsteady upwash as seen by the rotor blades at various thrusting conditions compared to the undisturbed boundary layer

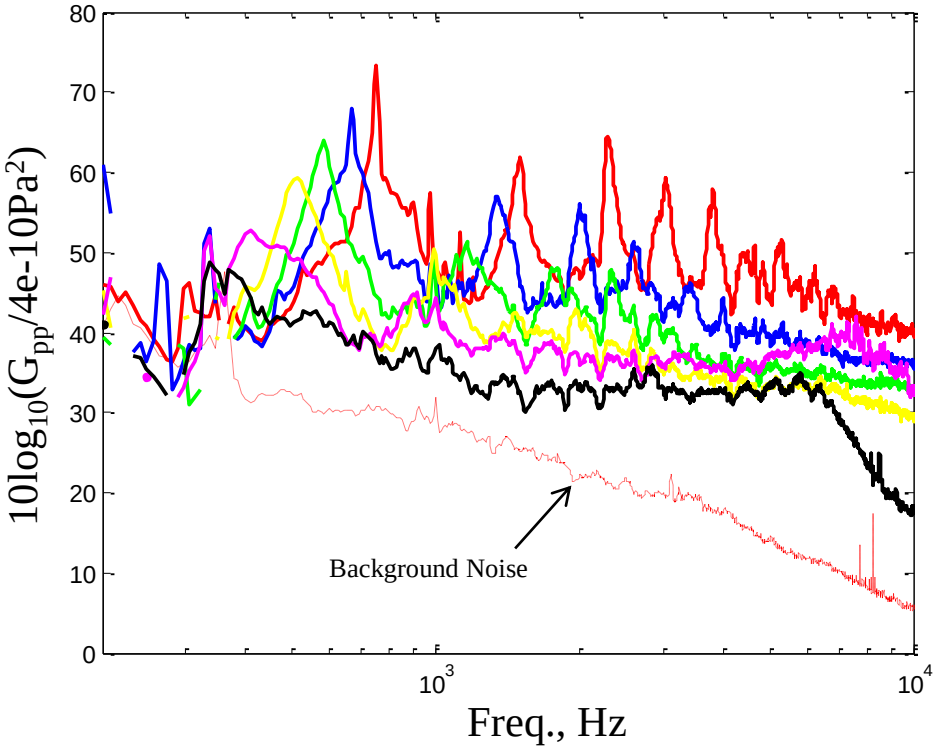

a)

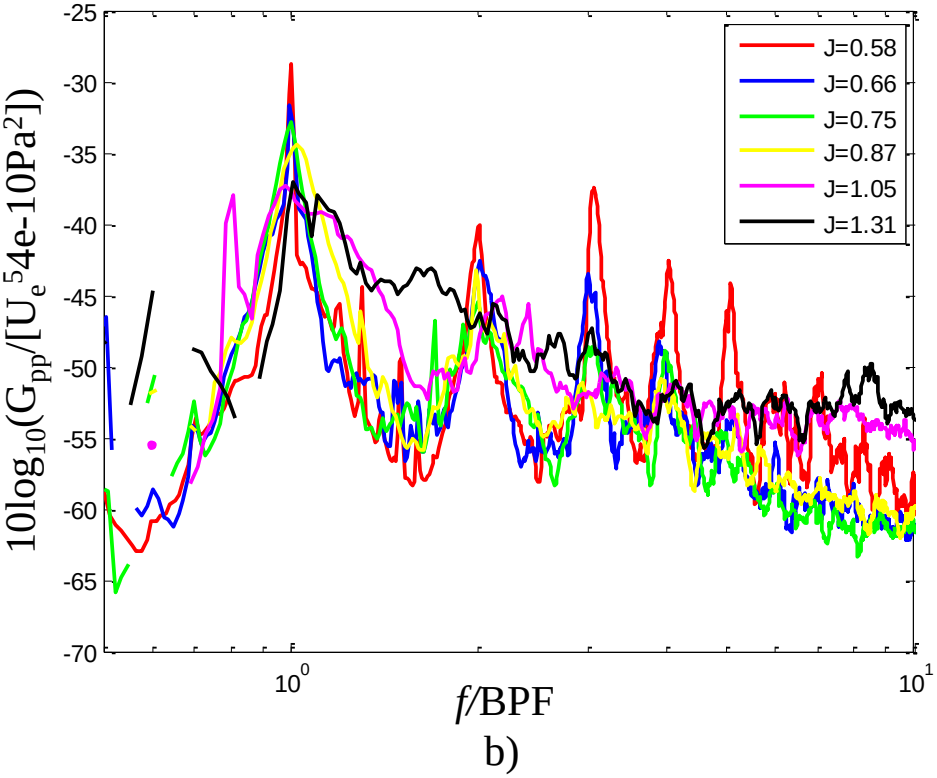

b)

Figure 11.a) Raw b) and normalized background-subtracted noise from the rotor operating in a 186 mm thick boundary layer with an inflow velocity of 20m/s

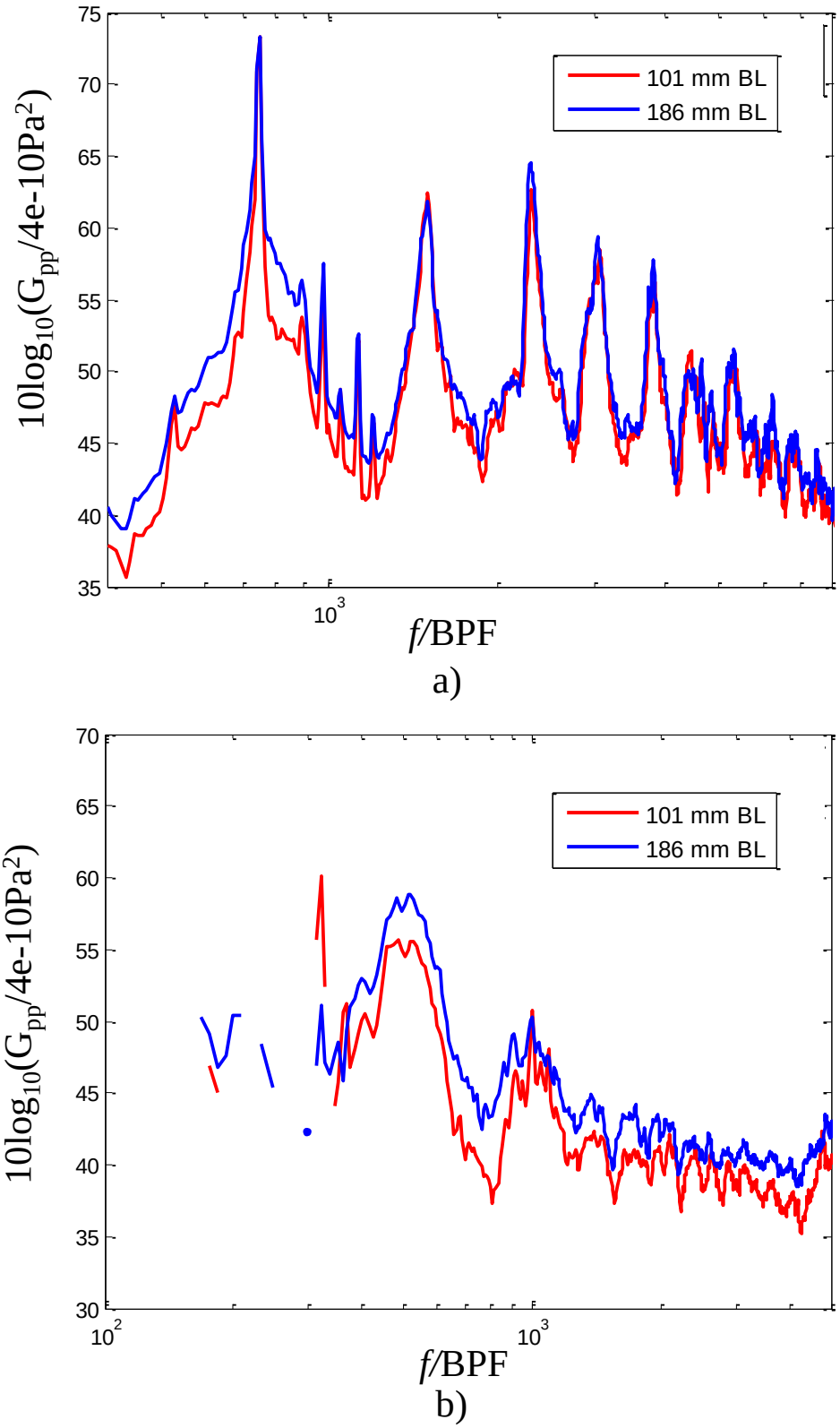

Figure 12.Comparison of noise measured from the rotor ingesting two different boundary layers, a) J =0.58 (20m/s, 4500 RPM) and b) J=1.44 (30m/s, 2734 RPM)

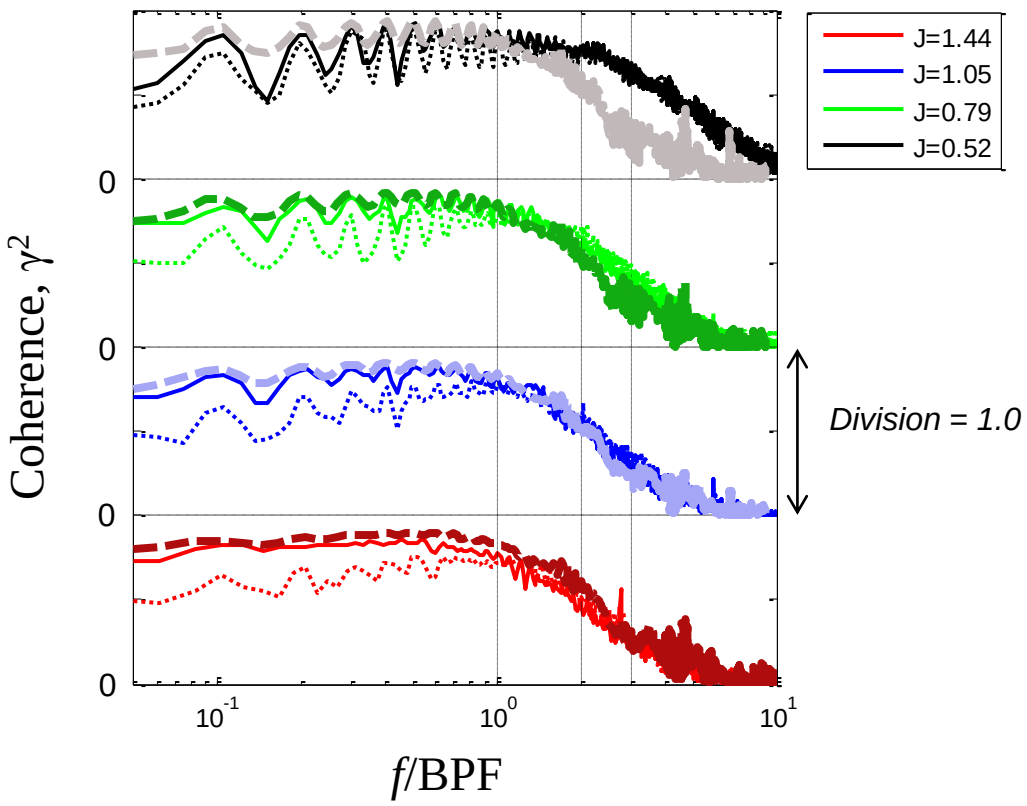

Figure 13.Comparison of unsteady upwash coherence for positions at 98.5%R and 95%R on the same blade for different thrusting conditions:186mm BL (solid), 101mm BL (dots), and prediction (dashed).